

Thermally induced ultrasonic emission from porous silicon

H. Shinoda, T. Nakajima, K. Ueno & N. Koshida

Department of Electrical & Electronic Engineering, Tokyo University of Agriculture & Technology, 2-24-16 Nakamachi, Koganei, Tokyo 184-8588, Japan

The most common mechanism¹ for generating ultrasound in air is via a piezoelectric transducer, whereby an electrical signal is converted directly into a mechanical vibration. But the acoustic pressure so generated is usually limited to less than 10 Pa, the frequency bandwidth of most piezoelectric ceramics is narrow, and it is difficult to assemble such transducers into a fine-scale phase array with no crosstalk^{2,3}. An alternative strategy using micromachined electrostatic diaphragms is showing some promise^{4,5}, but the high voltages required and the mechanical weakness of the diaphragms may prove problematic for applications. Here we show that simple heat conduction from porous silicon to air results in high-intensity ultrasound without the need for any mechanical vibrational system. Our non-optimized device generates an acoustic pressure of 0.1 Pa at a power consumption of 1 W cm⁻², and exhibits a flat frequency response up to at least 100 kHz. We expect that substantial improvements in efficiency should be possible. Moreover, as this material lends itself to integration with conventional electronic circuitry, it should be relatively straightforward to develop finely structured phase arrays of these devices, which would give control over the wavefront of the acoustic emissions.

The idea of a thermal sound generator (a “thermophone”) was proposed 80 years ago⁶, in which the acoustic element was a simple self-supporting, thin metal film. The photoacoustic effect in porous silicon has also been reported^{7,8}, but was used to characterize the porous silicon itself from gas expansion in a closed space. One might think that ultrasound generation by heat exchange is not possible, as

the thermal conduction is too slow. However, we report here that the experimental device shown in Fig. 1 operates as an efficient ultrasound emitter. It is composed of a patterned, thin aluminium film electrode (30 nm thick), a microporous silicon layer (10 μm thick), and a p-type crystalline silicon (c-Si) wafer. The porous silicon layer consists of many confined silicon nanocrystallites with three-dimensional nanopores⁹. In our experiment, the porous silicon layer (with porosity of ~70%) was formed by a conventional anodization technique in a solution of 55% HF:ethanol = 1:1 at a temperature of 20 °C at a current density of 20 mA cm⁻² for 8–40 min. The aluminium electrode was used to input a sinusoidal current into the porous silicon layer, the temperature of which was raised by Joule’s heating. The emitted acoustic pressure was measured as a function of output frequency by a microphone type 4138, Brüel & Kjør, Denmark) placed at a position of 3.5 cm from the front surface.

We now explain the device concept, based on a theoretical analysis of thermal conduction phenomena¹⁰ in the porous-silicon/air system as illustrated in Fig. 2a. Suppose that a thermal power density $q(\omega)\exp(j\omega t)$ (in units of W cm⁻²) with an angular frequency ω is provided at the surface of the porous silicon layer through a sufficiently thin metal film on it. When the thickness d of the porous silicon layer is such that

$$d > D \equiv \sqrt{\frac{2\alpha}{\omega C}} \quad (1)$$

where α and C are respectively the thermal conductivity and heat capacity per unit volume of porous silicon, then the surface temperature change $T_0(\omega)\exp(j\omega t)$ is given by

$$T_0(\omega) = \frac{q(\omega)}{\sqrt{j\omega\alpha C}} \quad (2)$$

if the expansion of porous silicon and the heat flow into the air are neglected (see Fig. 2b). The temperature change induces an acoustic pressure $P(x,\omega)\exp(j\omega t)$ through the alternating thermal expansion of the air. Using the fundamental equations of photoacoustic analysis¹¹, we find that

$$P(x, \omega) = A \frac{\exp(-jkx)}{\sqrt{\alpha C}} q(\omega), \quad A = \sqrt{\frac{\gamma\alpha_a}{C_a}} \frac{P_A}{vT_A} \quad (3)$$

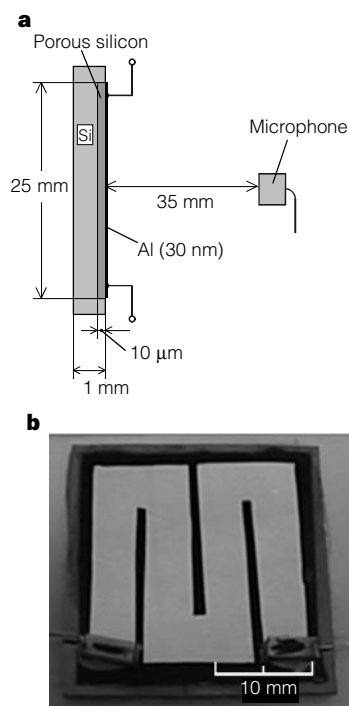


Figure 1 Our device for producing thermally induced ultrasonic emission. **a**, Cross-sectional view of the fabricated device and set-up for sound measurement. **b**, Photograph of a top view of our device.

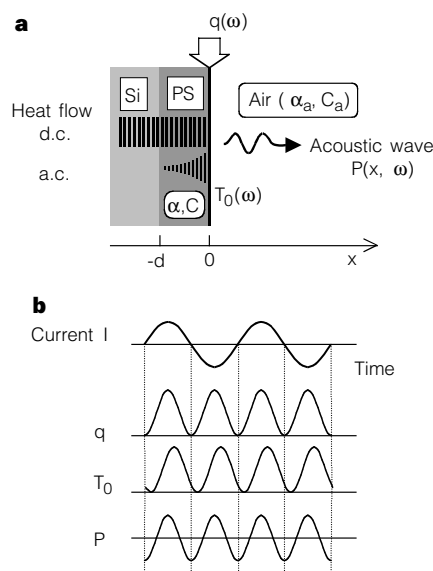


Figure 2 Device operation. **a**, The air/thin-Al-film porous-silicon (PS)/c-Si structure and the coordinate configuration. See text for details. **b**, current I introduced into the top electrode induces the surface temperature change T_0 by Joule’s heat q , which produces acoustic pressure P .

Table 1 Thermal properties of Si and SiO₂

	α (W m ⁻¹ K ⁻¹)	C (10 ⁶ J K ⁻¹ m ⁻³)	$\alpha C / (\alpha C)_{\text{c-Si}}$
c-Si	168	1.67	1
Porous silicon	1	0.7	1/400
SiO ₂	1.4	2.27	1/88

Shown are thermal conductivity, α , and heat capacity per unit volume, C , of c-Si in comparison to typical values for porous silicon. Data for SiO₂ are also shown for reference. Note that the relative value of the product αC of porous silicon is extremely low.

where P_A is atmospheric pressure, T_A is room temperature, v is the sound velocity, $\gamma = C_p/C_v = 1.4$, k is the wavenumber of free-space sound, α_a is the thermal conductivity of air, and C_a is the heat capacity per constant unit volume of air. The assumptions in this analysis are as follows: $k \ll \sqrt{\omega C_a / \alpha_a}$ (that is, the sound wavelength is much larger than thermal diffusion length), $\alpha C \gg \gamma \alpha_a C_a$ (that is, the heat flow into the device is much larger than that into the air), and the porous silicon itself does not vibrate. Too large a value of d causes a stationary temperature rise on the surface (which is useless for our purposes) and, in contrast, too small a d decreases the signal of the acoustic pressure amplitude itself. We note that the ratio $|P(\omega)|/|q(\omega)|$ is constant, and independent of ω . This means that an ideal, flat frequency response is expected from this device.

We now evaluate the product αC , because it determines the efficiency of the operation as suggested by equation (3). Table 1 shows typical thermal data of porous silicon in comparison to that of c-Si (refs 12, 13). The data of SiO₂ are also shown for reference. It is clear that the value of αC is $\sim 1/400$ that of c-Si: this big difference in αC between porous silicon and c-Si would prevent heat transfer of an alternating component to the inside of the device, while a possible stationary d.c. component would be quickly removed into the highly thermally-conductive c-Si substrate.

The measured acoustic pressure amplitudes are plotted in Fig. 3 as a function of output frequency for a sinusoidal Joule's heating power of 1 W cm^{-2} . A significantly high acoustic pressure is observed over a wide frequency range up to 100 kHz. The limit of upper measurement frequency at 100 kHz is simply due to the specification of our measurement system; and the condition of equation (1) is satisfied at frequencies above 5 kHz. As predicted by theory, sound intensity is independent of frequency in the high-frequency range where the wavelength is smaller than the device size, although some fluctuations caused by environmental reflection noise are seen. The value of the pressure also coincides with that calculated from equation (2) and the data in Table 1, as P (in Pa) = $0.07 \times q$ (in W cm^{-2}).

To compare (in Pa) the efficiency of our device with that of conventional methods is not straightforward, as the output acoustic pressure of our device is proportional to the input power per unit area, while that of piezoelectric or electrostatic devices is proportional to the input voltage. For conventional devices, an average membrane displacement of 12.6 nm V^{-1} at 1.7 MHz has been reported⁵: this corresponds to 55 Pa V^{-1} , which we take as the highest efficiency at present. A PZT bimorph transducer with impedance matching cone (EFRTUB50K5, Matsushita) generates 2 Pa V^{-1} at 40 kHz when it is measured at distance of 30 cm. In the survey by Manthey *et al.*,¹ typical efficiencies of both piezoelectric and (non-MEMS) electrostatic types are given as $0.1\text{--}1 \text{ Pa V}^{-1}$ at 200 kHz when measured at a distance of 1 m. (Here MEMS indicates micro-electrical-mechanical systems.) As the impedance of our experimental device was 5Ω , a 1 cm^2 device driven by a 5 V source gives a 0.4 Pa plane wave whose intensity is not much less than that of the conventional resonant device, though our device consumes more power. We note that the frequency range of our device is broad, unlike the resonant devices, and that its efficiency increases as the sound intensity increases. The thermo-acoustic coupling factor, which is defined as the square root of the ratio of the acoustic

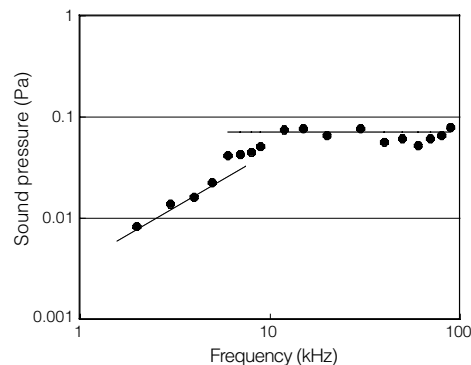


Figure 3 Experimental results. Shown is the measured acoustic pressure amplitude for the experimental device as a function of output frequency. The electrical power input was 1 W cm^{-2} . In the high-frequency range (where the wavelength is smaller than the device size), the sound pressure is independent of frequency, as predicted by theory.

power output to the input electric power, is 0.03% at 1 W cm^{-2} , while that of the conventional method reaches 10%. This low coupling factor is a present drawback of our non-optimized device. But the freedom to select its electrical impedance, and a high intensity free from the upper bound of conventional methods, are also advantages of our device, as are mechanical toughness, ideally flat frequency characteristics, and the potential to assemble a phased array of such devices with low crosstalk.

As a result of the scaling principle in thermal conduction phenomena, the use of dot electrode structures (in which the heat exchange is concentrated in small islands) should greatly improve the efficiency and output acoustic pressure of our devices. Moreover, such construction could prove useful in two-dimensional array fabrication because it provides a large wiring space. On the other hand, as suggested by the data in Table 1, the use of oxidized porous silicon would be a promising and practical approach to enhancing the efficiency.

Although we have not performed rigorous tests of its stability, this device is free from the often-quoted instability of porous silicon. The porous silicon layer is protected by the aluminium electrode from the atmosphere, and is not exposed to an intense electric field. (It is conceivable that oxidation might in fact upgrade the efficiency rather than degrade it.) We can confirm that this device worked well after three months at room temperature, humidity and pressure.

Particular attention has been paid to the visible luminescence of porous silicon^{14–16}. It is closely related to an optical bandgap widening, induced by strong quantum confinement in silicon nanocrystallites with the same band dispersions as c-Si (ref. 17). But complete carrier depletion in nanocrystallites associated with strong confinement, on the other hand, leads to extremely low values of α and C . The ability to control these parameters over a wide range, and the process compatibility with ultra-large-scale-integration (ULSI) technology—including a large difference in the thermal properties between porous silicon and c-Si—suggests applications of porous silicon in acoustic integrated devices. □

Received 18 January; accepted 13 July 1999.

- Manthey, W., Kroemer, N. & Magori, V. Ultrasonic transducers and transducer arrays for applications in air. *Meas. Sci. Technol.* **3**, 249–261 (1992).
- Mo, J. H., Fowlkes, J. B., Robinson, A. L. & Carson, P. L. Crosstalk reduction with a micromachined diaphragm structure for integrated ultrasonic transducer arrays. *IEEE Trans. Ultrasonics Ferroelectr. Freq. Control* **39**, 48–53 (1992).
- Goldberg, R. L. & Smith, S. W. Multilayer piezoelectric ceramics for two-dimensional array transducers. *IEEE Trans. Ultrasonics Ferroelectr. Freq. Control* **39**, 761–771 (1994).
- Soh, H. T., Atalar, A. & Khuri-Yakub, B. T. Surface micromachined capacitive ultrasonic transducers. *IEEE Trans. Ultrasonics Ferroelectr. Freq. Control* **45**, 678–690 (1998).
- Haller, M. I. & Khuri-Yakub, B. T. A surface micromachined electrostatic ultrasonic air transducer. *IEEE Trans. Ultrasonics Ferroelectr. Freq. Control* **43**, 1–6 (1998).
- Arnold, H. D. & Crandall, I. B. The thermophone as a precision source of sound. *Phys. Rev.* **10**, 22–38 (1917).

- Amato, G., Benedetto, G., Barino, L., Brunetto, N. & Spagnolo, R. Photothermal and photoacoustic characterization of porous silicon. *Opt. Eng.* **36**, 423–431 (1997).
- Calderon, A., Alvarado-Gil, J. J. & Gurevich, Y. G. Photothermal characterization of electrochemical etching processed n-type porous silicon. *Phys. Rev. Lett.* **79**, 5022–5025 (1997).
- Cullis, A. G., Canham, L. T. & Calcott, P. D. J. The structural and luminescence properties of porous silicon. *J. Appl. Phys.* **82**, 909–965 (1997).
- Holman, J. P. *Heat Transfer* (McGraw-Hill, New York, 1963).
- McDonald, F. A. & Wetsel, G. C. Jr Generalized theory of the photoacoustic effect. *J. Appl. Phys.* **49**, 2313–2322 (1978).
- Lang, W., Drost, A., Steiner, P. & Sandmaier, H. The thermal conductivity of porous silicon. *Mater. Res. Soc. Symp. Proc.* **358**, 561–566 (1995).
- Lang, W. in *EMIS Data Review Ser. no. 18, Properties of Porous Silicon* (ed. Canham, L.) 138–141 (IEE, London, 1997).
- Canham, L. Silicon quantum wire array fabrication by electrochemical and chemical dissolution of wafers. *Appl. Phys. Lett.* **57**, 1046–1048 (1990).
- Koshida, N. & Koyama, H. Visible electroluminescence from porous silicon. *Appl. Phys. Lett.* **60**, 347–349 (1992).
- Hirschman, K. D., Tsybeskov, L., Duttgupta, S. P. & Fauchet, P. M. Silicon-based visible light-emitting devices integrated into microelectronic circuits. *Nature* **384**, 338–341 (1996).
- Suda, Y., Obata, K. & Koshida, N. Band dispersions in photoluminescent porous silicon. *Phys. Rev. Lett.* **80**, 3559–3562 (1998).

Acknowledgements. We thank the late M. Fuchigami for his contribution to the analysis and experiments, and S. Ando who motivated this research. This work was partly supported by the Japan Society for the Promotion of Science, and a Grant-in-Aid for Scientific Research from the Ministry of Education, Science, Sports and Culture of Japan.

Correspondence and requests for materials should be addressed to H.S. (e-mail: shino@cc.tuat.ac.jp).

Layered double hydroxides exchanged with tungstate as biomimetic catalysts for mild oxidative bromination

Bert Sels*, Dirk De Vos*, Mieke Buntinx*, Frédéric Pierard†, A. Kirsch-De Mesmaeker† & Pierre Jacobs*

* Centre for Surface Chemistry and Catalysis, Katholieke Universiteit Leuven, 3001 Heverlee, Belgium

† Physical Organic Chemistry CP 160/08, Université Libre de Bruxelles, 1000 Bruxelles, Belgium

The manufacture of a range of bulk and fine chemicals, including flame retardants, disinfectants and antibacterial and antiviral drugs, involves bromination¹. Conventional bromination methods typically use elemental bromine, a pollutant and a safety and health hazard. Attempts to develop alternative and more benign strategies have been inspired by haloperoxidase enzymes, which achieve selective halogenation at room temperature and nearly neutral pH by oxidizing inorganic halides with hydrogen peroxide^{2,3}. The enzyme vanadium bromoperoxidase has attracted particular interest^{4,5} in this regard, and several homogeneous inorganic catalysts mimicking its activity are available^{6–11},

although they are limited by the requirement for strongly acidic reaction media. A heterogenous mimic operating at neutral pH has also been reported¹², but shows only modest catalytic activity. Here we describe a tungstate-exchanged layered double hydroxide that catalyses oxidative bromination and bromide-assisted epoxidation reactions in a selective manner. We find that the catalyst is over 100 times more active than its homogeneous analogue. The low cost and heterogeneous character of this system, together with its ability to operate efficiently under mild conditions using bromides rather than elemental bromine, raise the prospect of being able to develop a clean and efficient industrial route to brominated chemicals and drugs and epoxide intermediates.

Layered double hydroxides (LDH) consist of alternating cationic $M(II)_{1-x}M(III)_x(OH)_2^{x+}$ and anionic $A^{n-} \cdot zH_2O$ layers¹³. The positively charged layers contain edge-shared metal $M(II)$ and $M(III)$ hydroxide octahedra, with charges neutralized by A^{n-} anions located in the interlayer spacing or at edges of the lamellae. Small hexagonal LDH crystals with $M(II)_{1-x}Al_x(OH)_2(Cl)_x \cdot zH_2O$ composition (referred to as (MAL) LDH) were synthesized following existing procedures (here $M(II)$ is Mg ($x = 0.3$) or Ni ($x = 0.28$); the crystals were 50–100 nm in size with external surface areas of $\sim 100 \text{ m}^2 \text{ g}^{-1}$)¹³. Tungstate was exchanged onto chloride-saturated (MgAl) LDH or (NiAl) LDH to an extent of 12%. Chemical analysis showed complete uptake of the metal anion and release of equivalent amounts of chloride ions. X-ray powder diffraction patterns of the initial LDH materials and of the tungstate-exchanged LDH (WO_4^{2-} LDH) hardly differ in the range $2\theta = 3^\circ\text{--}65^\circ$. Lattice parameters calculated for rhombohedral symmetry $3R$ give c values of 2.346 and 2.376 nm ($3d_{001}$), and a values of 0.303 and 0.306 nm ($2d_{110}$) for (NiAl) LDH and (MgAl) LDH, respectively. The observed basal spacings remain unchanged after the anion exchange, which indicates that WO_4^{2-} should be mainly located in edge positions. Raman spectra of WO_4^{2-} LDH show vibrations (in cm^{-1}) at 345 (ν_2, ν_4), 838 (ν_3) and 931 (ν_1), characteristic for isolated tetrahedral tungstate (T_d)¹⁴. Hence there is no evidence for formation of polymeric tungsten compounds on the surface of the tungstate-exchanged LDHs that we used.

An assay for bromoperoxidase activity is the conversion of phenol red (phenolsulphonphthalein) into bromophenol blue (tetrabromophenolsulphonphthalein)^{4,5}. Conversion of 0.05 mM phenol red (wavelength of maximum absorption $\lambda_{\text{max}} = 429 \text{ nm}$) into bromophenol blue ($\lambda_{\text{max}} = 598 \text{ nm}$) was complete within 32 min in the presence of WO_4^{2-} (MgAl)LDH, 0.1 M NH_4Br and 2.5 mM H_2O_2 . This corresponds to 17 catalytic cycles in tungsten. The production of bromophenol blue presumably proceeds through H_2O_2 coordination on the metal and formation of peroxo-metal species. These were identified in the ultraviolet–visible reflectance spectra (for example, 330 nm for the tetraperoxo tungstate anion). When Br^- is added, the peroxo tungsten species react in

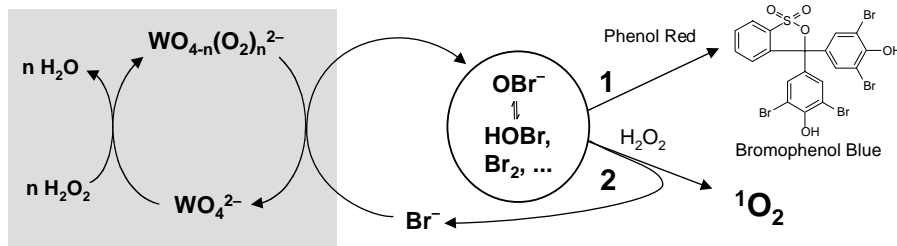


Figure 1 Catalytic cycle in bromination with WO_4^{2-} LDH. H_2O_2 binds to tungstate to form peroxotungstate at the surface of the LDH. Electrostatic attraction brings bromide to the surface, facilitating transfer of the activated oxygen atom from peroxotungstate to Br^- . Reactions of 2-electron-oxidized Br species in solution: electrophilic bromination of phenol red into bromophenol blue (route 1), and

bromide-assisted 1O_2 generation from H_2O_2 (route 2). A preparative experiment of (route 1) was run on a 250-ml scale, followed by work-up via extraction with ($n\text{-C}_6\text{H}_{13}$)₄NCl to a CH_2Cl_2 layer. The 1H NMR spectrum of the bromophenol blue product (7.29, s, 4H; 7.01 and 7.90, d, 1H each, $J = 7.5 \text{ Hz}$; 7.41 and 7.50, t, 1H each, $J = 7.5 \text{ Hz}$, TMS standard) is identical to that of authentic bromophenol blue.